



Published in final edited form as:

Nanotechnology. 2016 February 12; 27(6): 064001. doi:10.1088/0957-4484/27/6/064001.

A synergistic approach to the design, fabrication and evaluation of 3D printed micro and nano featured scaffolds for vascularized bone tissue repair

Benjamin Holmes¹, Kartik Bulusu¹, Michael Plesniak¹, and Lijie Grace Zhang^{1,2,3}

Lijie Grace Zhang: lgzhang@gwu.edu

¹Department of Mechanical and Aerospace Engineering, The George Washington University, Washington DC 20052, USA

²Department of Biomedical Engineering, The George Washington University, Washington DC 20052, USA

³Division of Genomic Medicine, Department of Medicine, The George Washington University Medical Center, Washington DC 20052, USA

Abstract

3D bioprinting has begun to show great promise in advancing the development of functional tissue/organ replacements. However, to realize the true potential of 3D bioprinted tissues for clinical use requires the fabrication of an interconnected and effective vascular network. Solving this challenge is critical, as human tissue relies on an adequate network of blood vessels to transport oxygen, nutrients, other chemicals, biological factors and waste, in and out of the tissue. Here, we have successfully designed and printed a series of novel 3D bone scaffolds with both bone formation supporting structures and highly interconnected 3D microvascular mimicking channels, for efficient and enhanced osteogenic bone regeneration as well as vascular cell growth. Using a chemical functionalization process, we have conjugated our samples with nano hydroxyapatite (nHA), for the creation of novel micro and nano featured devices for vascularized bone growth. We evaluated our scaffolds with mechanical testing, hydrodynamic measurements and *in vitro* human mesenchymal stem cell (hMSC) adhesion (4 h), proliferation (1, 3 and 5 d) and osteogenic differentiation (1, 2 and 3 weeks). These tests confirmed bone-like physical properties and vascular-like flow profiles, as well as demonstrated enhanced hMSC adhesion, proliferation and osteogenic differentiation. Additional *in vitro* experiments with human umbilical vein endothelial cells also demonstrated improved vascular cell growth, migration and organization on micro-nano featured scaffolds.

Keywords

3D printing; vascularized bone; nanomaterials; perfusable channel; stem cells; endothelial cells

1. Introduction

In recent years, 3D printing has become a popular and widely investigated method for the fabrication of large bone implants [1, 2]. 3D printed bone constructs, devices and treatments

hold great potential to repair traumatic and chronic injuries, restore tissue shape and function and return those afflicted with diseases and traumatic injury to large portions of bone (such as craniofacial and maxillofacial trauma) to normal, and even fully functional lives [3, 4]. Current work in academia has been very successful in applying 3D printing to design load bearing, patient specific and even to some degree bioactive bone constructs [5–10], but they have been limited in their ability to translate to clinically usable implants [11–13]. One of the most pressing reasons is that large and highly functioning areas of damaged bone, so called ‘critical defects,’ require an interconnected and effective vascular network [14, 15]. A dramatic example of such an injury would be someone who had severe damage to their skull and face, resulting from a car accident. But the need to grow large volumes of bone tissue can also extend to limb and total joint reconstruction, and is the sort of technology which would one day help to replace artificial limbs, orthotics and total joint replacement surgery. Solving this challenge is critical, as bone relies on an adequate network of blood vessels to transport waste, nutrients, growth factors and other chemicals and biological factors in and out of the tissue [14, 16, 17]. Bone tissue engineering has a specific need to solve this critical issue [18–23].

Today in the field nanostructured materials have already been popular for growth of blood vessels and biomimetic vascular networks to further enhance tissue growth [24–30]. Specifically, bone has been targeted as a model system for some of these studies. Sun *et al* modeled vascularized bone regeneration within a biodegradable nanoporous calcium phosphate scaffold loaded with growth factors [24]. Midha *et al* employed bioactive nanofeatured glass foam scaffolds to grow osteoblasts and vascular cells *in vitro* [25]. Both of these examples show how nanostructured materials can be used to effectively entice vascularized bone growth. On the opposite end, there are also benefits to designing larger support structures on the micro to macro scale which can initially support the functional aspects of vascularized bone, before and during new tissue formation. The ability to create highly ordered and interconnected anisotropic nano to micro to macro structures becomes especially important when designing multi-tissue systems, such as a vascular network growing throughout bone [26].

To this end, researchers have begun using 3D printing to create advanced macro-scale bone replacement implants and to create efficient, bioactive microfeatured networks [31–34]. Temple *et al* designed and produced anatomically shaped vascularized bone grafts with human adipose-derived stem cells and 3D-printed polycaprolactone scaffolds [4]. This demonstrated 3D printing’s ability to create devices for vascularized bone formation. However, there has been limited success thus far to print scaffold designs on the nanoscale [35, 36]. Combining nanostructured materials with micro and macro scaled 3D printing may hold the key to producing large yet fully functional and bioactive regenerative bone scaffolds, implants and devices.

Here we have combined nanomaterials and 3D printing for a highly innovative complex 3D printed scaffold with both nano and micro features for both bone and vascular growth. Key innovations of this project include the design and fabrication of a fully interconnected 3D fluid perfusable micro-channel network, within a microstructured bone forming matrix. Also in this study we designed and achieved a unique integration of nanocrystalline

hydroxyapatite (nHA) into our 3D printed scaffolds using a post fabrication process. We incorporated hydrodynamic measurement of unsteady pressure and flow rates. These measurements facilitate a preliminary understanding of the causal effects of predesigned structure-induced flow perturbations and the efficacy of such structures. Our motivation to study arterial blood flow in context of predesigned vascular structures is due to the essential role of blood supply for the growth of large critical-sized bone tissue. We envisioned that vascular network in the 3D printed scaffolds would experience flow conditions with some intrinsic vascular flow features such as flow rates, pressures and pulsatility. We therefore, modeled the hydrodynamic experiments under similar flow conditions in an exclusive arterial flow loop, recreating those salient cardiovascular flow characteristics. Ultimately, we believe that vascular flow properties and pulsatility may have a greater role to play toward fast, *in situ* delivery of blood, nutrients, progenitors and growth factors through our predesigned vascular structures. Cellular study was also conducted to prove scaffolds' effectiveness in enhancing cell growth and tissue formation, and physical characterization was performed to show desirable, bone like characteristics.

2. Methods

2.1. Scaffold design and 3D printing

Overall, we envision a novel strategy and efficacy for our designed scaffolds. Large microchannels (compared to smaller bone matrix microstructures) are intended to facilitate rapid blood diffusion throughout the scaffolds. This may be accomplished by exposure to blood or grafting of an adjacent arterial vessel during implantation. The purpose is to provide rapid and fully penetrating supplies of blood, nutrients and most importantly autologous cells *in situ*.

Figure 1 shows a flow chart of the overall experimental design. The scaffolds' outer shape was a 7.5 mm diameter and a 5 mm high cylinder. For the bone region, the scaffolds had a 250 μm diameter hexagonal pore size and a 375 μm layer height. The pores in the bone regions were closely packed and then stacked layer by layer, as opposed to the fluid flow microchannel networks which were long interconnected channels. In order to further dampen fluid perfusion through the bone matrix, and provide a more biomimetic network for microvascular vasculature to develop on, we sought to provide a disrupted, yet highly directionalized flow path perpendicular to the vertical alignment of the hexagonal pores through the scaffolds' pore structures by alternating the scaffold geometry between a simple line pattern and a hexagonal pore pattern. That is to say, the first layer of scaffold pore structure was an arrangement of interlocking hexagons in the *X-Y* plane, while moving up another full layer in the *Z*-direction the pore structure changes to a simple series of aligned struts. This pattern then alternates between hexagons and struts with each layer.

The mechanism of pore geometry on cell development has been recently shown to be a product of the total pore perimeter size, rather than the explicit pore shape [37]. Still, the 'hexagonal shape' as it is realized here may provide an opportunity to create 3D printed hexagonal pores that are smaller than the smallest printable square pores. Within this bone matrix, a series of interconnected horizontal and vertical channels were designed, in order to provide a fast and efficient perfusion of arterial blood throughout the scaffold architecture

(figures 2(A)–(G)). The ‘bone’ region porosity is shown in gray, while the microchannels are outlined in red. In our designs the channel diameter was also varied between a 500 and a 250 μm radius. All scaffold 3D models were then saved as stl files and processed using the Slic3r software package and saved as gcodes. They were then subsequently printed from polylactic acid (PLA) on a Solidoodle fused deposition modeling printer in a layer by layer fashion using the Pronterface software controller interface. Additionally, representative CAD models of the scaffolds’ porosity were made using Rhino, and then analyzed for surface area, volume, and pore density.

2.2. nHA synthesis and aminolysis functionalization

After initial 3D fabrication, scaffolds were additionally modified with a nHA conjugation. nHA was first synthesized using a wet chemistry procedure and a hydrothermal process, as thoroughly described in our previous studies [38, 39]. Then, nHA particles were conjugated onto scaffolds using a process described by Aishwarya *et al* [40] and our previous study [41]. First, PLA scaffolds were aminolysed. This was achieved by immersing them in an ethylenediamine/*n*-propanol (1:9 ratio) solution at 60 °C for 5 min. Scaffolds were then extensively washed with deionized water and dried at 35 °C. This results in the presence of an NH_2 amine group on the PLA substrate. The aminolysed scaffolds were then immersed in a 1% glutaraldehyde solution at room temperature for 3 h to conjugate CHO functional groups onto the NH_2 groups. After washing extensively, scaffolds were immersed in a solution of 10% w/v nHA at 4 °C for 24 h. The process itself yields a series of layered chemical attachments, which includes an NH_2 amino group attached to the PLA, CHO functional groups formed off of the amines and finally nHA conjugated on the CHO functional groups.

2.3. Mechanical testing and scaffold characterization

Five scaffolds from both microchannel groups were tested. Scaffolds were tested using a Lucas Scientific FLS-I portable mechanical tester. A 3 cm compression platen was fitted to the advancing end of the piston, and scaffolds were compressed at a strain rate of 0.1 cm min^{-1} , until failure. Data was collected and analyzed in Excel. The slope of the linear elastic region of each sample’s produced stress strain graph was calculated in order to find the Young’s Modulus. Samples were imaged using a Zeiss SigmaVP scanning electron microscope (SEM). Scaffolds were coated with a roughly 10 nm thick conductive gold layer using a gold sputter coater. Scaffolds were then imaged using 3.65 kV electron beam. Additionally, scaffold which were not coated with gold were mounted on carbon tape and analyzed using an Oxford instruments energy dispersive x-ray (EDX) spectroscope, in order to characterize the elemental composition present on scaffolds’ surfaces.

2.4. Hydrodynamic measurements of flow rate and pressure

Hydrodynamic experiments and data collection were performed using a custom made, 180° curved artery test section (with curvature ratio, $r/R = 1/7$) setup designed to represent a dynamically similar pulsatile arterial blood flow through a single arterial vessel [42–46]. The closed loop experimental setup shown in figure 3, consists of a fluid reservoir, inlet and outlet pipes, a programmable pump and a 180° curved tube test section. The inlet and outlet pipes are made of acrylic and approximately, 2 m long and are connected to a removable

180° curved test section. A Newtonian blood-analog fluid is supplied using a programmable pump (ISMATEC BVP-Z) to tubes containing the scaled model-scaffolds. The inflow conditions are based on a carotid artery-based digitized flow rate waveform reported in a paper by Holdsworth *et al* [47]. The composition of the Newtonian blood-analog fluid used in experiments is 40% glycerine and 60% deionized water (by weight). The kinematic viscosity of $3.4449 (\pm 0.071\ 246) \text{ mm}^2 \text{ s}^{-1}$ was measured using a standard Ubbelohde viscometer and density (1.078 g ml^{-1}) at approximately 27 °C (ambient room temperature) [42–46].

2.5. In vitro study

hMSCs were obtained from the Texas A&M Health Science Center, Institute for Regenerative Medicine, and were expanded originally from a donor source. Additionally, human umbilical vein endothelial cells (HUVECs) were purchased from Life Technologies. All hMSC studies were cultured in complete cell media (CCM) consisting of alpha minimum essential medium, 16% fetal bovine serum, 1% L-glutamine, and $10 \mu\text{g ml}^{-1}$ of ciprofloxacin. hMSC osteogenic differentiation studies were cultured in CCM supplemented with $50 \mu\text{g ml}^{-1}$ L-ascorbate acid (Sigma) and 10 mM β -glycerophosphate (Sigma). HUVECs were cultured in endothelial growth media consisting of medium 200 and 2% low serum growth supplement both purchased from Life Technologies. hMSC and HUVEC *in vitro* studies on our constructs were conducted as follows.

For hMSC and HUVEC adhesion, printed bone scaffolds were seeded with 50 000 cells per scaffold. Sample groups included scaffolds with large and small microchannels, and scaffolds with large and small microchannels conjugated with nHA. Samples were cultured in 24 well plates for 4 h, and then transferred to new well plates, washed twice with phosphate buffered solution (1X) and trypsinized with 0.25% trypsin EDTA in an incubator for 6 min. This time period was decreased for HUVECs to 3 min, at room temperature. Suspensions were then aliquoted into a 96 well plate. $100 \mu\text{l}$ of each sample suspension were reacted with a molecular probes MTS cell counting reagent and incubated at 37 °C for 1 h. Samples were then read on a Thermo Scientific Multiskan GO photometric plate reader at 490 nm. hMSC and HUVEC proliferation was conducted at 1, 3 and 5 d. Samples were seeded with 55 000 cells per scaffold, cultured in CCM and counted at each time point using the same MTS assay described above.

hMSC differentiation studies were seeded with 125 000 cells per scaffold and cultured for three weeks. At the end of each week, samples were taken from each experimental group and digested via a papain digestion protocol consisting of a PBS wash, freezing in a $-80 \text{ }^{\circ}\text{C}$ freezer and drying overnight in a lyophilizer. Samples were then immersed in $500 \mu\text{l}$ papain and incubated at 60 °C for 24 h. Samples once digested were tested for calcium and collagen type I deposition. A calcium detection kit was used to test samples for calcium deposition. $200 \mu\text{l}$ of suspension were removed from each sample, transferred to a 96 well plate and reacted with a dye reagent, after being reacted with an acidic calcium dissociation reagent. Once the reaction was complete, samples were read on a photometric plate reader at a detection wavelength of 560 nm. A collagen type I ELISA immunochemistry assay was used to measure collagen type I content. $50 \mu\text{l}$ of solution from each sample were transferred to a

96 well plate, washed with a dissociation reagent, and transferred to a 96 well plate coated with capture antibodies (standard ELISA assay wellplate). After incubation at 37 °C, samples remaining solutions was removed from the wells, and they were washed. A second dye-bound antibody was transferred to the wells, and the plate was incubated at 37 °C. The wells were then emptied, washed, and a dissociation reagent was added. Samples were then read on a photometric plate reader at a 490 nm detection wavelength.

2.6. Confocal microscopy

Fluorescent labeling and confocal imaging were also used to further characterize hMSC spreading and morphology on our constructs. Special 0.5 mm thick scaffolds were fabricated and then seeded with 500 000 hMSCs cells per scaffold. Samples were taken at 1, 3 and 5 d, fixed in formalin for 15 min and treated with 0.1% Triton-X for 15 min to permeate the cell membrane. Samples were then stained with Texas Red- phalloidin for 15 min and stained with DAPI for 10 min. Samples were viewed on a Zeiss 710 confocal microscope. HUVECs were also seeded, cultured and imaged, similar to the protocol above. They were also stained with a Texas Red—phalloidin preparation which was a 1:40 concentration of dye methanol stock to PBS, as opposed to a 1:200 dilution used for hMSC staining. This was to ensure that the HUVECs, which are smaller and grow in less dense groups than hMSCs, were completely stained and visible. In order to jump start angiogenesis, the printed samples were further treated with a 100 ng ml⁻¹ concentration of human vascular endothelial growth factor (VEGF₁₂₁, a highly effective and proven growth factor responsibly for new vessel formation [48, 49]) at 37 °C for 24 h, prior to cell culture. Additionally, once angiogenesis starts, cells growing in the microenvironment often continually express VEGF as new blood vessels are forming [50–52], which is why we chose not to include it as an additive in the cell media.

2.7. Statistics

All quantitative material testing and cellular studies were conducted with either a sample size of $n = 3$ or three repeated experiments with total samples size of $n = 9$ per group for each time point, respectively. All quantitative data was compared using a student's t-test, with a p value less than 0.05 taken as 'statistically significant.'

3. Results

3.1. Characterization of 3D printed bone scaffold with fluid perfusable microchannel network

SEM imaging (figures 4(A)–(D)) showed that we were able to print vertical microchannels, within a porous bone matrix, with both a 500 and 250 μm radius. In addition, SEM imaging of partially printed scaffolds showed the successful fabrication of aligned and interconnected horizontal channels. Once PLA 3D printed scaffolds were fabricated, they were subsequently chemically conjugated with nHA. Scaffolds with nHA were imaged via SEM at high resolution (figures 4(E) and (F)). In addition, figure 4(G) shows a spectrograph of the elemental analysis obtained from EDX. The graph clearly shows the presence of peaks consistent with and identified by the instrument's analysis software as Calcium. Table 1 shows physical attributes calculated using Rhino and Excel, and compares them to values computed from measured scaffold dimensions taken from SEM images. The table

demonstrates that we could print scaffolds to within tens of microns of the designed microstructural measurements, and thus achieve relatively comparable physical scaffolds characteristics. It also shows that we were able to effectively change the channel diameter, while keeping the porosity and surface area to volume ratio fairly constant.

Mechanical testing data demonstrated that scaffolds printed with PLA in our predesigned vascularized bone microstructures could withstand normal mechanical loading, and exhibited typical elastic behavior (figure 5). The Young's Modulus of scaffolds printed with smaller microchannels was 51% higher than those printed with larger channels. While both scaffolds performed within the regime less than normal cortical bone in compression (10–50 GPa) [53–55], they still fall within the range of recorded failure regimes of bone under impact loading [56, 57]. The behavior of a material when more void space, (i.e. larger confined spaces with no material or structure present) is introduced suggests that the scaffolds with larger channels would in fact have diminished mechanical properties [53].

3.2. Hydrodynamic flow characterization of scaled-microchannels

Scaffold models that were scaled to match the hydrodynamic measurement-setup (figure 3) were subjected to pulsatile, carotid artery-based inflow conditions. The pulsatile inflow waveforms were scaled using dynamic similarity to a time period (T) of 4 s, while maintaining the signal harmonics and minimization of Gibbs-type phenomenon using a data acquisition card (NI-USB6229). Details of experimental inflow conditions and parameters such as mean and maximum Reynolds numbers, pulsation harmonics, dynamic scaling can be found in papers by Glenn *et al* [45, 46] Bulusu and Plesniak [42–44]. The mean and maximum Reynolds numbers maintained at the same level as the waveform reported in the paper by Holdsworth *et al* [47].

The pressure and flow rate associated with the inflow waveform were measured using a pressure catheter with an optimally damped MEMS cantilever (Transonic Scisense™) and an ultrasonic flow rate sensor (Transonic ME12PXL), respectively. The location of these sensors are shown in figure 3.

One hundred cycles of pressure and flow rate were measured to generate a statistically relevant data ensemble at 250 Hz (sampling frequency i.e., 1000 waveform instances acquired over a 4 s time period, T). The data collected from one hundred measurement cycles was adequate for the production of phase averaged pressure and flow rate. Pressure and flow rate could then be used for phase-shift related discussions. MATLAB™ was used for all data processing, as described above.

In order to investigate the fluid flow behavior of different diameter channels, a 'clean artery-control case' (vessel with no construct) and two scaled up models representing an isolated section of the scaffolds' scaled-microchannel network were designed using Rhino, and 3D printed on a Stratasys Objet24 Desktop 3D printer (figure 6(A)). These constructs were then inserted into the system detailed above (figure 6(B)) at two locations from the 180° curved tube test section, viz., at the inlet of the 180° curved tube test section and in the straight inlet pipe away from the 180° curved tube test section.

Self-normalized pressure and flow rate data plotted against the dimensionless time ($0 \leq t/T \leq 1$) are shown in figures 7(A)–(E) to enable a direct comparison for temporal, pressure and flow rate variations and, phase shifts. The measured waveforms downstream from the test section showed a flow rate and pressure signals with phase shifts or delays that progressively increase during on full cycle of the inflow waveform. This pressure-flowrate delay or phase shift is representative of blood flow in vessels without any obfuscations such as stenoses and prosthetics such as stents or scaffolds and accordingly, we called it the clean artery-control case. The results of our measurements are further divided into five cases by the type of channel and location as shown in figures 7(A)–(E); This phase-shift phenomenon generally, can be seen with the constructs were placed at two locations (proximity to and away from the test section) and is pronounced after the peak of the waveforms (known as systolic peak) and during the deceleration phase. The flow rate and pressure waveforms for the large and small diameter scaled-microchannels demonstrated subtle, but observable phase-shifts (between $0.18 \leq t/T \leq 0.3$). The measurements though preliminary, revealed that despite the presence of the constructs there is minimal variation in pressure-flow rate phase-shifts in comparison with the control case.

3.3. Enhanced hMSC and HUVEC growth and development in 3D printed nHA conjugated microstructured bone constructs

Initial adhesion studies showed that after 4 h, hMSC cellular adhesion decreased on scaffolds without nHA when the size of the microchannels decreased (figure 8(A)). After adding nHA, small channel scaffolds were 4.6% more adherent than the scaffolds with the least number of adhered cells (small channels with no nHA). Proliferation studies yielded increases at 1 and 3 d (figure 8(B)). After 5 d of culture, scaffold with small microchannels and nHA had the highest cell number, with a 39% increase compared to the large micro-channel scaffold with no nHA, and a 51% increase when compared to the scaffolds with large microchannels and nHA.

We performed further confocal imaging experiments on hMSCs proliferating on our scaffolds for 5 d (figure 9). After only 1 d of culture, hMSCs formed dense and evenly distributed networks of aligned cells on all scaffolds. On scaffolds with $250 \mu\text{m}$ microchannels, cells formed cell aggregates, which appeared to have more dense and aligned morphologies. These effects were in turn greatly enhanced on scaffolds that were conjugated with nHA. Additional increased cell growth and enhanced arrangement could be seen on nHA conjugated scaffolds with $250 \mu\text{m}$ micro-channels over 3 and 5 d of culture.

HUVEC *in vitro* evaluation showed that our scaffolds are also effective in supporting and enhancing vascular cell growth and activity. 4 h HUVEC adhesion demonstrated that HUVEC cells adhere the best on scaffolds with small channel diameters and nHA (figure 10(A)). Specifically, the small microchannel scaffold with nHA had a 43.7% greater cell count than the least performing scaffold. HUVEC 5 day proliferation showed increases in cell number at 1, 3 and 5 d (figure 10(B)), with the greatest increase on the scaffolds without nHA and with large microchannels, which was a staggering 201% greater when compared to the least performing group (small nHA conjugated). Confocal imaging of cultured HUVECs (figure 11) showed HUVECs adhering and growing on scaffolds after 1, 3 and 5 d. After 1 d,

Author Manuscript

dense cellular aggregates can be observed on the large channel scaffolds, and some appear to be forming long micro-tubular vessels aligned with the scaffold's geometry. Scaffolds with smaller channels have less present cell populations, but exhibited similar morphology. Scaffolds with nHA and VEGF did not show the same sort of high cellular activity, specifically with regard to the formation of long, continuous, interconnected vascular tubes. Additionally, a strong fluorescent background signal from the nHA modification made it difficult to accurately assess total HUVEC morphology. But, due to observable cell nuclei, cells attaching and forming zig-zag patterns could be observed on the actual surface of scaffold features. At 3 and 5 d, cell aggregates broke up and HUVECs continued to form long vascular structures and networks along the features of the large channels scaffolds. Comparatively, cells continued to form zig-zagging cellular arrangements and denser aggregates on the scaffolds with small channels, conjugated with nHA and a pre culture VEGF treatment.

Author Manuscript

hMSC osteogenic differentiation study results are shown in figures 12(A) and (B). Collagen type I synthesis (figure 12(A)) was significantly increased on scaffolds with nHA, as compared to those without, after 1 week. Additionally, all scaffolds increased after three weeks, with the greatest increase being on the scaffolds with small channels and nHA. Specifically, scaffolds with small microchannels and nHA showed a 13% increase over scaffolds with large microchannels and no nHA conjugation. Additional calcium deposition (figure 12(B)) increased in calcium on all scaffolds, and the greatest calcium increase being on the scaffolds with nHA and smaller microchannels. There was an increase in calcium deposition from the large channels design to the small channel scaffold. At 2 and 3 weeks of culture, calcium deposition on small channel scaffolds with nHA was greatly enhanced. These scaffolds had a 391% increase over scaffolds with large channels and no nHA. After 3 weeks both scaffold with nHA had similar calcium content and overall was the dominant factor in upregulating calcium deposition after longer periods of time. However, at two weeks the scaffolds with small channels and nHA were the only scaffold to show significant calcium deposition, demonstrating the ability of smaller channels to entice earlier calcium deposition upregulation.

4. Discussion

4.1. Biomimetic physical and hydrodynamic properties on 3D printed scaffolds

Author Manuscript

In this study, a series of well-defined microfeatured bone scaffold were printed, within the well-established resolution for 3D printing [58–60]. Post fabrication nHA was readily and effectively applied to our scaffolds using a aminolysis based conjugation process [41]. This allowed us to effectively create a highly novel micro and nano featured scaffold for enhanced bone and vascular cell growth. Our scaffolds also performed in compression, comparably to natural bone [53, 54, 61]. These results showed that as the size of blood vessel microchannels was decreased, the Young's Modulus increased. However, this is due to the reduction of void space in the scaffold structure, and this is a well-known structural phenomenon in material science and solid mechanics [41, 53, 62]. All of these results demonstrate very plainly that we were able to design and fabricate scaffolds to highly

specified and bone-like characteristics, and these scaffolds then exhibited bone-like physical, particularly mechanical, properties.

As previously discussed, a blood supply is essential for the growth of large critical sized bone tissue. Some researchers in the field have begun utilizing flow perfusion bioreactors, to influence different cell types to form highly structured, micro-vascularized bone [63, 64]. But, these methods rely on extensive *in vitro* or *ex vivo* culture of tissues before they can be theoretically used clinically. Therefore, it is highly clinically relevant to design a scaffold, implant or orthopedic regenerative construct for vascularized, critical sized bone defects which can quickly and efficiently generate an arterial blood flow throughout. This would allow for fast *in situ* delivery of blood, nutrients, progenitors and growth factors either through fluid perfusion or arterial grafting to the implant. The supply of pulsatile arterial blood through the proposed microchannels would then diffuse through the smaller, more biomimetic porous matrix, allowing for the development of vascularized bone tissue. Thus, we sought to evaluate preliminary hydrodynamic performance through our scaffold designs, to get a better idea of scaffold performance with regard to this desired effect on blood flow and body fluid introduction. The experimental setup shown in figure 3, has been successfully used for cardiovascular flow diagnostics under stenotic and stent-implanted conditions that are believed to occur in physiological and clinical environments [42–44]. We performed preliminary hydrodynamic measurements of pulsatile pressure and flow rates in this setup and compared them to a control case (see figures 7(A)–(E)). We hypothesize that microvascular mimicking structures that maintain temporal, pressure-flow rate phase shifts as those characterized in native blood vessels would constitute an effectively designed structure.

The pressure and flow rate waveforms have similar temporal profiles such as characteristic systolic and diastolic phases and intrinsic phase shifts or time delays. These phase shifts are certain instances very subtle and sensitive to the scaffold location; compare perforated lines in figures 7(B)–(E). The scaled-channel designed structures, having large and small channels exhibited this phase shifting phenomenon, in a manner highly comparable and correlated to the clean artery –control case. This observation suggests that hydrodynamics of the designed micro-vessels may have the same characteristics as the control case representing native vessels with arterial blood flow. Accordingly, such designed structures may provide efficient and adequate blood and fluid transport in and out of the scaffold, without causing any flow disruptions to the system. Our future studies will rigorously evaluate these insights.

In summary, the hydrodynamic measurements have led to the integration of flow diagnostics with microchannel structure designs and have provided the means to evaluate the efficacy of vascularized bone constructs. The main implication of these measurements is that microchannel structures can be designed to generate flow characteristics that are highly correlated to native vascular systems, and may profile effective flow fluid perfusion and blood flow.

4.2. Enhanced cellular response and bone formation

Our scaffolds exhibited excellent performance during all hMSC study, and greatly enhanced both calcium and collagen type I synthesis during hMSC osteogenic differentiation.

Specifically, scaffolds with smaller channels and nHA performed the best. Since these scaffolds had physical and chemical properties most closely associated with native vascularized bone, we expected them to elicit the most bone formation and osteogenic differentiation [26, 65, 66]. Specifically this was due in part to adequate, yet more physiologically comparable fluid transfer, mechanical properties and both chemical and nanostructural contributions of the nHA. There was a slight decrease in collagen type I deposition on nHA scaffolds after 2 weeks of culture, but collagen type I content increased again after 3 weeks. This may have been due to enhanced cellular migration on nHA conjugated scaffolds, as initial cellular migration and invasion has been shown to suppress both proliferation and tissue deposition, temporarily [41, 67–69].

HUVEC adhesion showed good initial attachment on scaffold with small channels and conjugated nHA. However, 5 d proliferation, while showing good increase in cell number on all scaffolds, had a large spike on the large channel scaffolds without nHA after 5 d. When these scaffolds were imaged with a confocal microscope, they also showed the greatest density of cells, and the most developed vascular structures. This may have been for several reasons. All vascular endothelial cell types rely heavily on fluid flow and shear stresses to migrate, grow, and align to form new tissue [70, 71]. And while they also may leverage structural cues for growth, this is a dominant factor in development. Our scaffolds were cultured in static conditions, which may show different cell growth and vascular formation behavior, as compared to fluid flow conditions (such as in a bioreactor) [72, 73]. However, it is important to consider a static condition, since our constructs would be initially implanted into a large bone defect, and not directly into blood vessels with available pumping arterial blood. The increased access to nutrients and chemicals in culture, and the potential for convective fluid mixing in scaffolds with larger microchannel spaces may have contributed to micro-shears in the fluid environment which could have effected cell growth [74]. HUVECs are also a very potent cell type [72, 73], and the presence of a softer substrate (no nHA) for cell attachment and more free space may have caused a high amount of HUVECs to grow more rapidly.

According to confocal imaging, all scaffolds showed highly enhanced hMSC attachment and spreading. 3D printed scaffolds displayed well integrated and highly aligned cell growth, displaying the effectiveness of these scaffolds to promote cellular organization. A decrease in size of our microchannels had denser, even more highly aligned cellular aggregates. Continued culture on scaffolds with small channels and conjugated nHA displayed increasing cell density, as well as larger and more spread cytoskeletons and filopodia. HUVECs which were also cultured on scaffold with small channels and nHA developed well after 5 d. Cells grew in dense, at times zig-zagging arrangements across scaffold features' surfaces. Despite the fact that larger, longer and more highly developed vascular structures could be seen on pure PLA scaffolds with large diameter channel networks, vascular growth was mostly only observed in the 3D printed channels, pores and between scaffold features, whereas HUVECs could be seen growing on the full surface of nHA conjugated scaffolds. This demonstrated that nHA conjugated scaffold could direct efficient and effective growth and development within 3D printed structures.

5. Conclusion

In this project, a new, detailed construct for bone and vascular development was designed and validated. This design relies on complex, anisotropic structures designed to support hMSC osteogenic differentiation and bone formation, as well as vascular cell growth. In addition, nHA was successfully conjugated onto scaffolds post fabrication, for a highly novel combination of both bone and biomimetic microchannel structures, and osteogenic nanofeatures. Scaffolds had physical properties comparable to bone fracture regimes, and flow measurements revealed that the designed microchannels had similar flow characteristics to native blood vessels. Enhanced hMSC adhesion and growth were observed on scaffolds with small microchannels and nHA modification while scaffolds with large channels promoted the greatest HUVEC growth. MSC osteogenic differentiation study indicates our 3D printed scaffolds have excellent bone forming potential, based on collagen type I and calcium content. When all of the evaluated factors are taken into account, scaffolds with both large and small microchannels and nHA may provide a powerful construct for further *in vitro* experiments where multiple cell types are co-cultured, or for future *in vivo* study.

Acknowledgments

This work is supported by NIH Director's New Innovator Award 1DP2EB020549-01 and GW Institute for Biomedical Engineering Research Fund. No. competing financial interests exist.

References

1. Cooke MN, Fisher JP, Dean D, Rimnac C, Mikos AG. Use of stereolithography to manufacture critical-sized 3D biodegradable scaffolds for bone ingrowth. *J Biomed Mater Res B*. 2003; 64:65–9.
2. Haberstroh K, et al. Bone repair by cell-seeded 3D-bioplotting composite scaffolds made of collagen treated tricalciumphosphate or tricalciumphosphate-chitosan-collagen hydrogel or PLGA in ovine critical-sized calvarial defects. *J Biomed Mater Res B*. 2010; 93:520–30.
3. Shim JH, et al. Three-dimensional printing of rhBMP-2-loaded scaffolds with long-term delivery for enhanced bone regeneration in a rabbit diaphyseal defect. *Tissue Eng A*. 2014; 20:1980–92.
4. Temple JP, et al. Engineering anatomically shaped vascularized bone grafts with hASCs and 3D-printed PCL scaffolds. *J Biomed Mater Res A*. 2014; 102:4317–25. [PubMed: 24510413]
5. Seitz H, Rieder W, Irsen S, Leukers B, Tille C. Three-dimensional printing of porous ceramic scaffolds for bone tissue engineering. *J Biomed Mater Res B*. 2005; 74:782–8.
6. Khalyfa A, et al. Development of a new calcium phosphate powder-binder system for the 3D printing of patient specific implants. *J Mater Sci Mater Med*. 2007; 18:909–16. [PubMed: 17216579]
7. Habibovic P, Gbureck U, Doillon CJ, Bassett DC, van Blitterswijk CA, Barralet JE. Osteoconduction and osteoinduction of low-temperature 3D printed bioceramic implants. *Biomaterials*. 2008; 29:944–53. [PubMed: 18055009]
8. Klammert U, Vorndran E, Reuther T, Muller FA, Zorn K, Gbureck U. Low temperature fabrication of magnesium phosphate cement scaffolds by 3D powder printing. *J Mater Sci Mater Med*. 2010; 21:2947–53. [PubMed: 20740307]
9. Klammert U, Gbureck U, Vorndran E, Rodiger J, Meyer-Marcotty P, Kubler AC. 3D powder printed calcium phosphate implants for reconstruction of cranial and maxillofacial defects. *J Cranio-Maxillo-Facial Surg*. 2010; 38:565–70.
10. Warnke PH, et al. Ceramic scaffolds produced by computer-assisted 3D printing and sintering: characterization and biocompatibility investigations. *J Biomed Mater Res B*. 2010; 93:212–7.

11. Obregon F, Vaquette C, Ivanovski S, Hutmacher DW, Bertassoni LE. Three-dimensional bioprinting for regenerative dentistry and craniofacial. *Tissue Engineering. J Dental Res.* 2015; 29:002203451558885.
12. Hollister SJ, et al. Design control for clinical translation of 3D printed modular scaffolds. *Ann Biomed Eng.* 2015; 43:774–86. [PubMed: 25666115]
13. Gibbs DM, Vaezi M, Yang S, Oreffo RO. Hope versus hype: what can additive manufacturing realistically offer trauma and orthopedic surgery? *Regenerative Med.* 2014; 9:535–49.
14. Barralet J, Gbureck U, Habibovic P, Vorndran E, Gerard C, Doillon CJ. Angiogenesis in calcium phosphate scaffolds by inorganic copper ion release. *Tissue Eng A.* 2009; 15:1601–9.
15. Vogelien E, Jones NF, Huang JI, Brekke JH, Lieberman JR. Healing of a critical-sized defect in the rat femur with use of a vascularized periosteal flap, a biodegradable matrix, and bone morphogenetic protein. *J Bone Joint Surg Am.* 2005; 87:1323–31. [PubMed: 15930543]
16. Remagen W. The bone cell system: form and function. *Beitrage zur Pathologie.* 1973; 150:1–10. [PubMed: 4358466]
17. Lozano AJ, Cestero HJ Jr, Salyer KE. A comparative study of the early vascularization of porous carbon and bone as a graft. *J Biomed Mater Res.* 1976; 10:545–8. [PubMed: 780357]
18. Schaefer D, et al. Tissue-engineered composites for the repair of large osteochondral defects. *Arthritis Rheumatism.* 2002; 46:2524–34. [PubMed: 12355501]
19. Vunjak-Novakovic G, Meinel L, Altman G, Kaplan D. Bioreactor cultivation of osteochondral grafts. *Orthodontics Craniofacial Res.* 2005; 8:209–18.
20. Oliveira JM, et al. Novel hydroxyapatite/chitosan bilayered scaffold for osteochondral tissue-engineering applications: scaffold design and its performance when seeded with goat bone marrow stromal cells. *Biomaterials.* 2006; 27:6123–37. [PubMed: 16945410]
21. Wang M, Cheng X, Zhu W, Holmes B, Keidar M, Zhang LG. Design of biomimetic and bioactive cold plasma-modified nanostructured scaffolds for enhanced osteogenic differentiation of bone marrow-derived mesenchymal stem cells. *Tissue Eng A.* 2013; 20:1060–71.
22. Holmes B, Castro NJ, Zhang LG, Zussman E. Electrospun fibrous scaffolds for bone and cartilage tissue generation: recent progress and future developments. *Tissue Eng B.* 2012; 18:478–86.
23. Zhang L, Webster, Thomas J. Nanotechnology and nanomaterials: promises for improved tissue regeneration. *Nano Today.* 2009; 4:66–80.
24. Sun X, Kang Y, Bao J, Zhang Y, Yang Y, Zhou X. Modeling vascularized bone regeneration within a porous biodegradable CaP scaffold loaded with growth factors. *Biomaterials.* 2013; 34:4971–81. [PubMed: 23566802]
25. Midha S, van den Bergh W, Kim TB, Lee PD, Jones JR, Mitchell CA. Bioactive glass foam scaffolds are remodelled by osteoclasts and support the formation of mineralized matrix and vascular networks *in vitro*. *Adv Healthc Mater.* 2013; 2:490–9. [PubMed: 23184651]
26. Fedorovich NE, De Wijn JR, Verbout AJ, Alblas J, Dhert WJ. Three-dimensional fiber deposition of cell-laden, viable, patterned constructs for bone tissue printing. *Tissue Eng A.* 2008; 14:127–33.
27. Farokhi M, Mottaghitalab F, Ai J, Shokrgozar MA. Sustained release of platelet-derived growth factor and vascular endothelial growth factor from silk/calcium phosphate/PLGA based nanocomposite scaffold. *Int J Pharmaceutics.* 2013; 454:216–25.
28. Wang S, et al. Evaluation of 3D nano-macro porous bioactive glass scaffold for hard tissue engineering. *J Mater Sci Mater Med.* 2011; 22:1195–203. [PubMed: 21445655]
29. Kobayashi H, et al. Vascular-inducing poly(glycolic acid)-collagen nanocomposite-fiber scaffold. *J Biomed Nanotechnol.* 2013; 9:1318–26. [PubMed: 23926797]
30. Santos MI, et al. Endothelial cell colonization and angiogenic potential of combined nano- and micro-fibrous scaffolds for bone tissue engineering. *Biomaterials.* 2008; 29:4306–13. [PubMed: 18706689]
31. Cohen A, Laviv A, Berman P, Nashef R, Abu-Tair J. Mandibular reconstruction using stereolithographic 3-dimensional printing modeling technology. *Oral Surg Oral Med Oral Pathol Oral Radiol Endodontics.* 2009; 108:661–6.
32. Cui X, Boland T. Human microvasculature fabrication using thermal inkjet printing technology. *Biomaterials.* 2009; 30:6221–7. [PubMed: 19695697]

33. Moon S, et al. Layer by layer three-dimensional tissue epitaxy by cell-laden hydrogel droplets. *Tissue Eng C*. 2010; 16:157–66.
34. Curodeau A, Sachs E, Caldarise S. Design and fabrication of cast orthopedic implants with freeform surface textures from 3D printed ceramic shell. *J Biomed Mater Res*. 2000; 53:525–35. [PubMed: 10984701]
35. Rengier F, et al. 3D printing based on imaging data: review of medical applications. *Int J Comput Assisted Radiol Surg*. 2010; 5:335–41.
36. Visconti RP, Kasyanov V, Gentile C, Zhang J, Markwald RR, Mironov V. Towards organ printing: engineering an intra-organ branched vascular tree. *Expert Opin Biol Ther*. 2010; 10:409–20. [PubMed: 20132061]
37. Rumpler M, Woesz A, Dunlop JW, van Dongen JT, Fratzl P. The effect of geometry on three-dimensional tissue growth. *J R Soc Interface*. 2008; 5:1173–80. [PubMed: 18348957]
38. Wang M, Cheng X, Zhu W, Holmes B, Keidar M, Zhang LG. Design of biomimetic and bioactive cold plasma-modified nanostructured scaffolds for enhanced osteogenic differentiation of bone marrow-derived mesenchymal stem cells. *Tissue Eng A*. 2014; 20:1060–71.
39. Castro NJ, O'Brien C, Zhang LG. Biomimetic biphasic 3D nanocomposite scaffold for osteochondral regeneration. *AIChE J*. 2014; 60:432–42.
40. Aishwarya S, Mahalakshmi S, Sehgal PK. Collagen-coated polycaprolactone microparticles as a controlled drug delivery system. *J Microencapsulation*. 2008; 25:298–306. [PubMed: 18465301]
41. Holmes B, Zhu W, Li J, Lee JD, Zhang LG. Development of novel three-dimensional printed scaffolds for osteochondral regeneration. *Tissue Eng A*. 2015; 21:403–15.
42. Bulusu, KV.; Plesniak, MW., editors. In plastico investigation of flow rate pressure phas-shifts toward arterial secondary flow structure dynamics. 4th Int. Conf. on Experimental Fluid Mechanics 2014; Beijing, China. 12–15 August; 2015.
43. Bulusu KV, Hussain S, Plesniak MW. Determination of secondary flow morphologies by wavelet analysis in a curved artery model with physiological inflow. *Exp Fluids*. 2014; 55:1–20.
44. Bulusu KV, Plesniak MW. Secondary flow morphologies due to model stent-induced perturbations in a 180° curved tube during systolic deceleration. *Exp Fluids*. 2013; 54:1–13.
45. Glenn AL, Bulusu KV, Shu F, Plesniak MW. Secondary flow structures under stent-induced perturbations for cardiovascular flow in a curved artery model. *Int J Heat Fluid Flow*. 2012; 35:76–83.
46. Glenn, A.; Shu, F.; Bulusu, KV.; Plesniak, MW., editors. Secondary flow structure under stent-induced perturbations for cardiovascular flow in a curved artery model. 7th Int. Symp. on Turbulence and Shear Flow Phenomena; 2011; Ottawa, Canada. 28–31 July; 2011.
47. Holdsworth DW, Norley CJ, Frayne R, Steinman DA, Rutt BK. Characterization of common carotid artery blood-flow waveforms in normal human subjects. *Physiol Meas*. 1999; 20:219–40. [PubMed: 10475577]
48. King TW, Patrick CW Jr. Development and *in vitro* characterization of vascular endothelial growth factor (VEGF)-loaded poly(DL-lactic-co-glycolic acid)/poly (ethylene glycol) microspheres using a solid encapsulation/single emulsion/solvent extraction technique. *J Biomed Mater Res*. 2000; 51:383–90. [PubMed: 10880080]
49. Hojo M, et al. Induction of vascular endothelial growth factor by fibrin as a dermal substrate for cultured skin substitute. *Plastic Reconstructive Surg*. 2003; 111:1638–45.
50. Ogasawara S, et al. Expression of angiogenic factors, basic fibroblast growth factor and vascular endothelial growth factor, in human biliary tract carcinoma cell lines. *Hepatology Res*. 2001; 20:97–113.
51. Grellier M, Ferreira-Tojais N, Bourget C, Bareille R, Guillemot F, Amedee J. Role of vascular endothelial growth factor in the communication between human osteoprogenitors and endothelial cells. *J Cell Biochem*. 2009; 106:390–8. [PubMed: 19127540]
52. Li H, et al. The role of vascular actors in two dimensional dialogue of human bone marrow stromal cell and endothelial cell for inducing self-assembled network. *PloS One*. 2011; 6:e16767. [PubMed: 21304816]
53. Fan H, et al. Modulus-density scaling behaviour and framework architecture of nanoporous self-assembled silicas. *Nat Mater*. 2007; 6:418–23. [PubMed: 17515915]

54. Holmes B, Castro NJ, Li J, Keidar M, Zhang LG. Enhanced human bone marrow mesenchymal stem cell functions in novel 3D cartilage scaffolds with hydrogen treated multi-walled carbon nanotubes. *Nanotechnology*. 2013; 24:365102. [PubMed: 23959974]
55. Lambers FM, Bouman AR, Rinnac CM, Hernandez CJ. Microdamage caused by fatigue loading in human cancellous bone: relationship to reductions in bone biomechanical performance. *PLoS One*. 2013; 8:e83662. [PubMed: 24386247]
56. Mow VC, Ratcliffe A, Rosenwasser MP, Buckwalter JA. Experimental studies on repair of large osteochondral defects at a high weight bearing area of the knee joint: a tissue engineering study. *J Biomech Eng*. 1991; 113:198–207. [PubMed: 1875694]
57. Flachsman ER, Broom ND, Oloyede A. A biomechanical investigation of unconstrained shear failure of the osteochondral region under impact loading. *Clin Biomech*. 1995; 10:156–65.
58. Cui X, Breitenkamp K, Finn MG, Lotz M, D'Lima DD. Direct human cartilage repair using three-dimensional bioprinting technology. *Tissue Eng A*. 2012; 18:1304–12.
59. Muller M, Becher J, Schnabelrauch M, Zenobi-Wong M. Printing thermoresponsive reverse molds for the creation of patterned two-component hydrogels for 3D cell culture. *J Vis Exp*. 2013; 10:e50632.
60. Murugesan K, Anandapandian PA, Sharma SK, Vasantha Kumar M. Comparative evaluation of dimension and surface detail accuracy of models produced by three different rapid prototype techniques. *J Indian Prosthodontic Soc*. 2012; 12:16–20.
61. Premnath K, Sridevi J, Kalavathy N, Nagarajan P, Sharmila MR. Evaluation of stress distribution in bone of different densities using different implant designs: a three-dimensional finite element analysis. *J Indian Prosthodontic Soc*. 2013; 13:555–9.
62. Cranford SW, Buehler MJ. In silico assembly and nanomechanical characterization of carbon nanotube buckypaper. *Nanotechnology*. 2010; 21:265706. [PubMed: 20534890]
63. Salter E, Goh B, Hung B, Hutton D, Ghone N, Grayson WL. Bone tissue engineering bioreactors: a role in the clinic? *Tissue Eng B*. 2012; 18:62–75.
64. Grayson WL, et al. Engineering anatomically shaped human bone grafts. *Proc Natl Acad Sci USA*. 2010; 107:3299–304. [PubMed: 19820164]
65. Celik M, Tuncer S, Emekli U, Kesim SN. Histologic analysis of prefabricated, vascularized bone grafts: an experimental study in rabbits. *J Oral Maxillofacial Surg*. 2000; 58:292–5. discussion 6.
66. Nguyen LH, et al. Vascularized bone tissue engineering: approaches for potential improvement. *Tissue Eng B*. 2012; 18:363–82.
67. Nakayama KH, Hou L, Huang NF. Role of Extracellular Matrix Signaling Cues in Modulating Cell Fate Commitment for Cardiovascular. *Tissue Eng Adv Healthc Mater*. 2014; 3:628–41.
68. Meng E, et al. High mobility group box 1 protein inhibits the proliferation of human mesenchymal stem cells and promotes their migration and differentiation along osteoblastic pathway. *Stem Cells Dev*. 2008; 17:805–13. [PubMed: 18715162]
69. Granero-Molto F, et al. Regenerative effects of transplanted mesenchymal stem cells in fracture healing. *Stem Cells*. 2009; 27:1887–98. [PubMed: 19544445]
70. Leclerc E, Furukawa KS, Miyata F, Sakai Y, Ushida T, Fujii T. Fabrication of microstructures in photosensitive biodegradable polymers for tissue engineering applications. *Biomaterials*. 2004; 25:4683–90. [PubMed: 15120514]
71. Lee VK, et al. Creating perfused functional vascular channels using 3D bio-printing technology. *Biomaterials*. 2014; 35:8092–102. [PubMed: 24965886]
72. Pirlo RK, Wu P, Liu J, Ringeisen B. PLGA/hydrogel biopapers as a stackable substrate for printing HUVEC networks via BioLP. *Biotechnol Bioeng*. 2012; 109:262–73. [PubMed: 21830203]
73. Andukuri A, et al. A hybrid biomimetic nanomatrix composed of electrospun polycaprolactone and bioactive peptide amphiphiles for cardiovascular implants. *Acta Biomaterialia*. 2011; 7:225–33. [PubMed: 20728588]
74. Morini GL. Viscous heating in liquid flows in micro-channels. *Int J Heat Mass Transfer*. 2005; 48:3637–47.

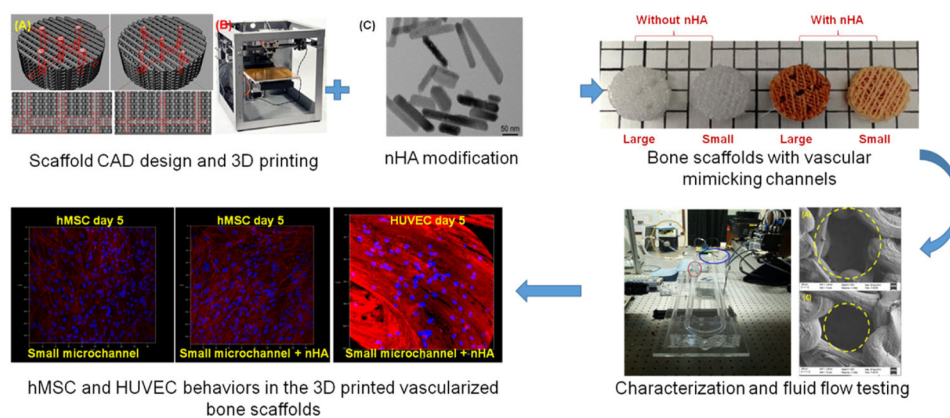


Figure 1.
Flow chart showing the overall experimental design.

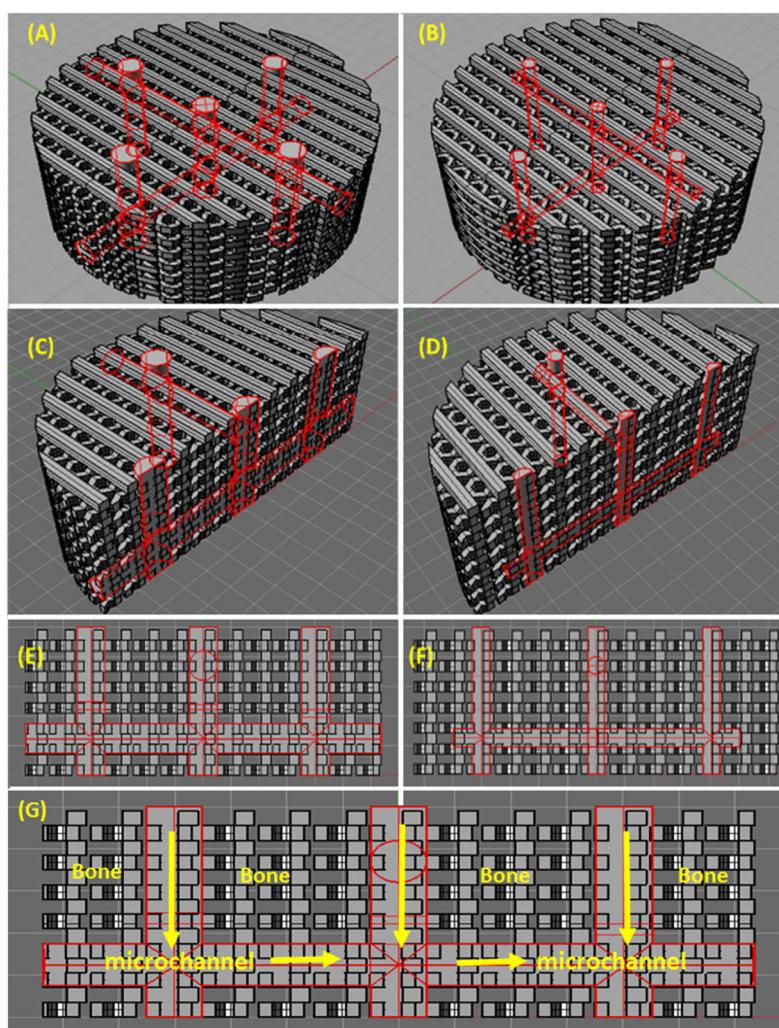


Figure 2. 3D CAD modeling of scaffolds with (A), (C), (E) 500 μm microchannels and (B), (D), (F) 250 μm microchannels. (G) illustrates the flow patterns in the microchannels of the designed scaffolds.

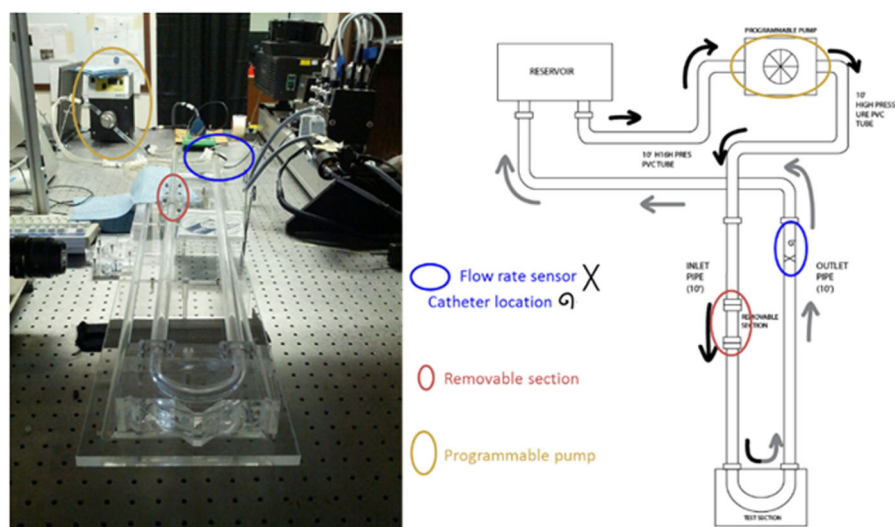


Figure 3.

Image and schematic illustration of experimental pulsatile flow setup. The black arrows represent the upstream fluid flow, or fluid being moved through the system and to the test section. The gray arrows represent the downstream flow, or fluid moving past the test section and returning through the system to the fluid reservoir.

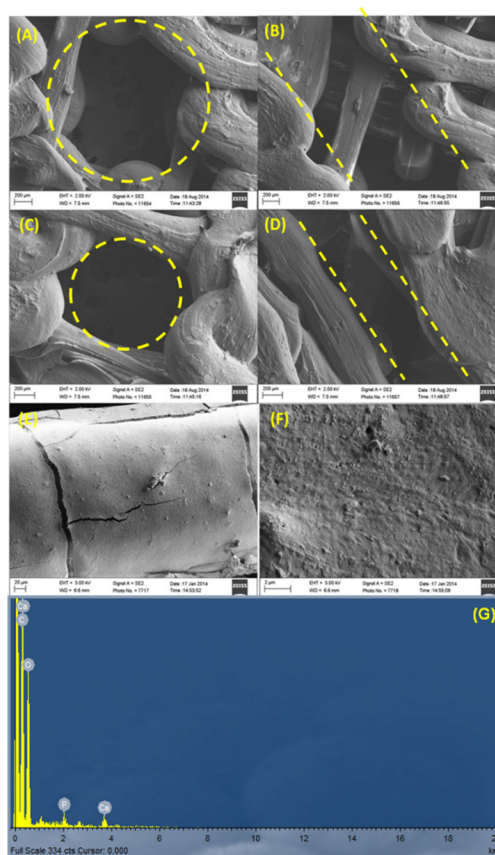


Figure 4.

SEM images of 500 μm (A) vertical and (B) horizontal channels, and 250 μm (C) vertical and (D) horizontal pores, (E) low magnification and (F) high magnification SEM images of the surface of a nHA conjugated PLA 3D printed scaffold. (G) EDX analysis of the nHA modified scaffold.

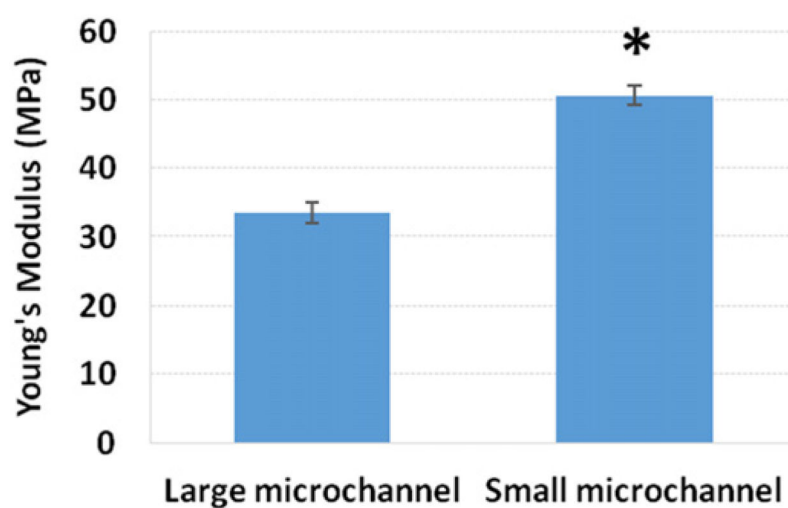


Figure 5. Young's modulus of mechanically compressed scaffolds, Data are mean \pm standard error of the mean, $n = 5$; * $p < 0.05$ when compared to large vascular mimicking channel scaffolds.

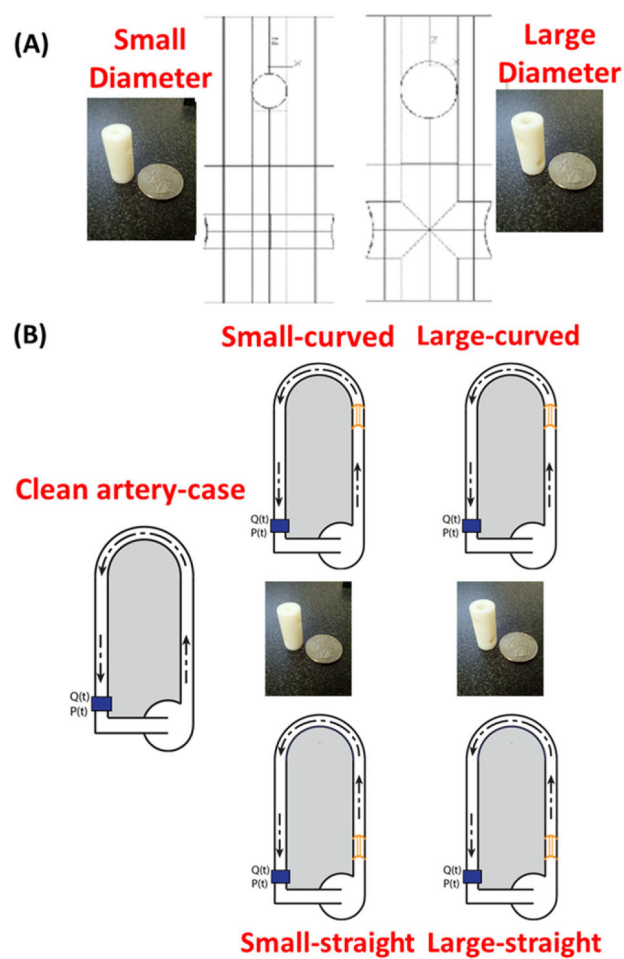


Figure 6.
Illustrations of the flow experiment for all five test cases.

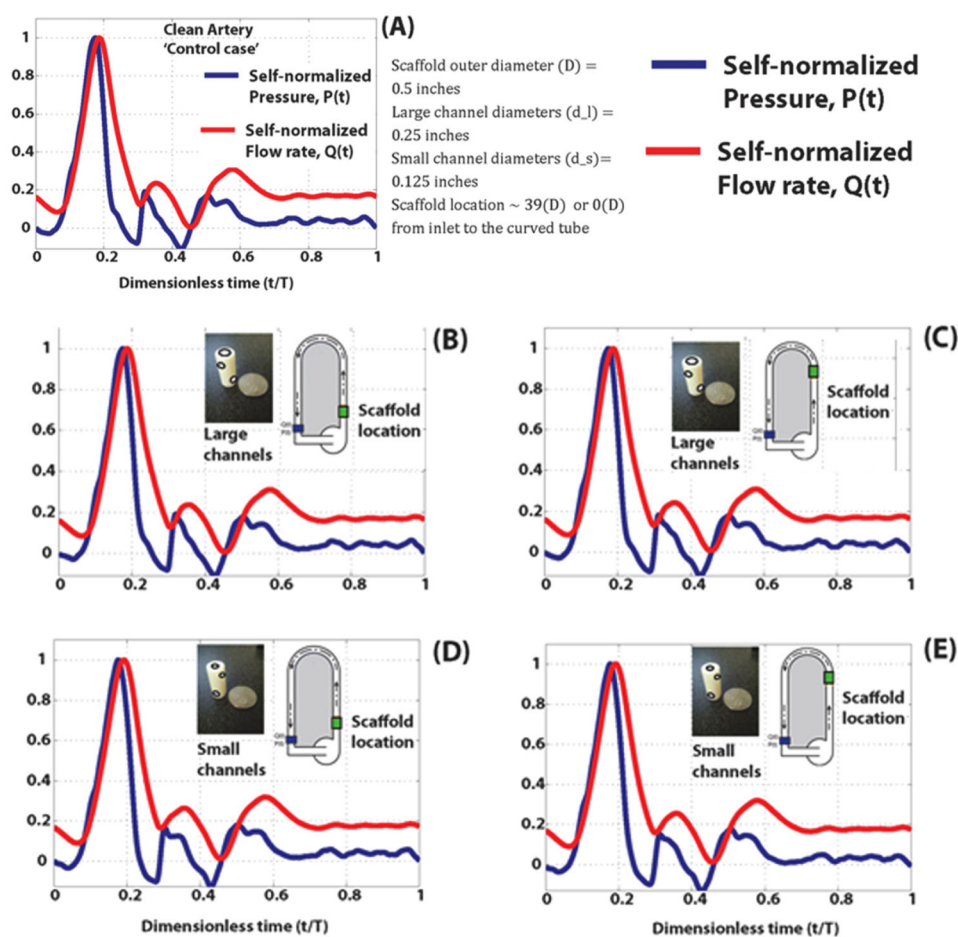


Figure 7.

Experimental flow mechanics, pressure (blue) and flow rate (red) analysis of the (A) clean artery control, (B) large channel models and (D) small channel models placed in a straight pipe and (C) large channel models and (E) small channel models placed in a curved pipe. All values are normalized for comparison, and are not the true measured experimental values.

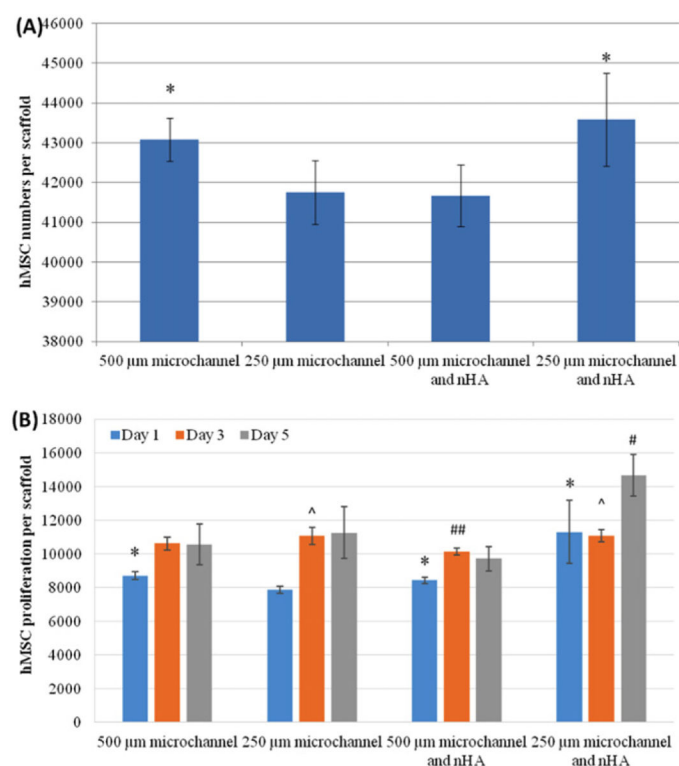


Figure 8.

(A) hMSC adhesion on 3D printed scaffolds; data are mean \pm standard error of the mean, $n = 9$; * $p < 0.05$ when compared to scaffolds with 250 μm microchannels and with 500 μm microchannels and nHA. (B) Improved hMSC proliferation on 3D printed scaffolds with nHA and small microchannels; data are mean \pm standard error of the mean, $n = 9$; # $p < 0.01$ when compared to all other scaffolds at day 5 and ## $p < 0.05$ when compared to 500 and 250 μm microchannels without nHA; ^ $p < 0.05$ when compared to scaffolds with 500 μm microchannels and nHA at day 3; and * $p < 0.05$ when compared to scaffolds with 250 μm microchannels at day 1.

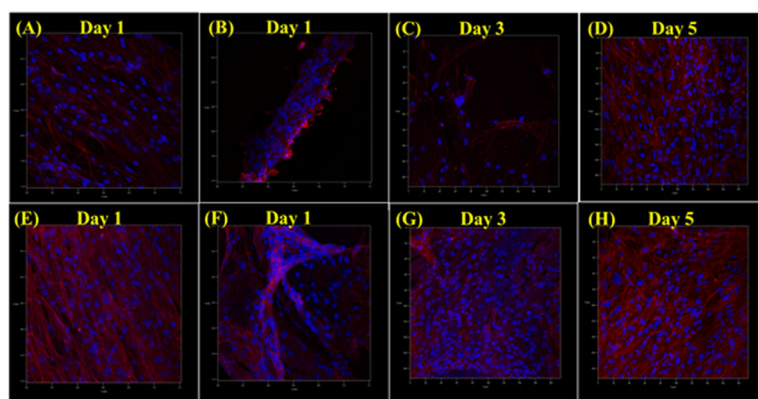
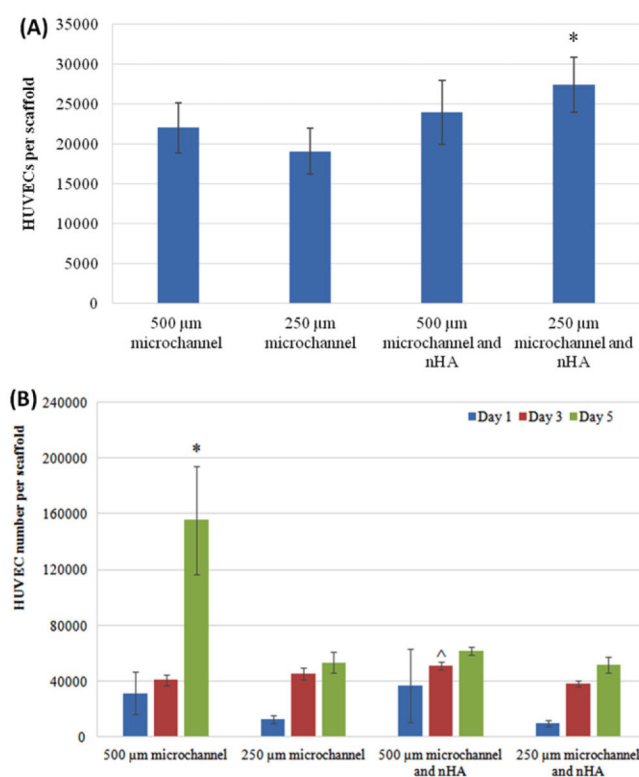


Figure 9.

Confocal microscopy images of 1 d hMSC growth on scaffolds with (A) 500 μm microchannels, (B) 250 μm microchannels, (E) 500 μm microchannels + nHA, (F) 250 μm microchannels + nHA, and 3 and 5 d hMSC growth on scaffolds with (C) and (D) 250 μm microchannels and (E) and (F) 250 μm microchannels + nHA.

**Figure 10.**

HUVEC adhesion; data are mean \pm standard error of the mean, $n = 9$; * $p < 0.05$ when compared to scaffolds with 250 μm microchannels. HUVEC proliferation on 3D printed scaffolds; data are mean \pm standard error of the mean, $n = 9$; * $p < 0.05$ when compared to all other scaffolds at day 5; and $\wedge p < 0.05$ when compared to scaffolds with 500 μm microchannels and 250 μm microchannels with nHA at day 3.

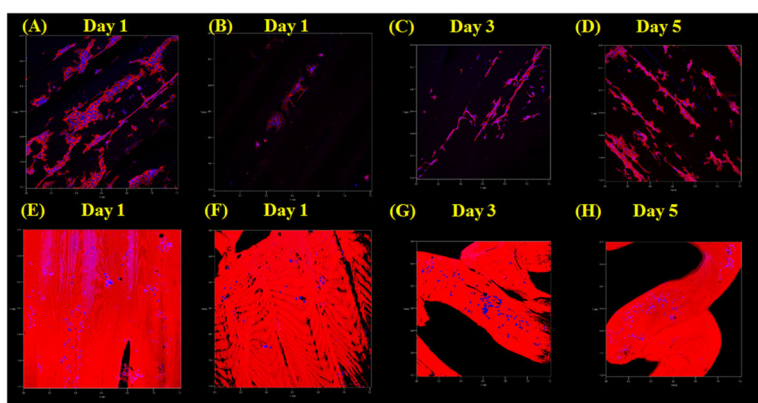


Figure 11.

Confocal microscopy images of 1 d HUVEC growth on scaffolds with (A) 500 μm microchannels, (B) 250 μm microchannels, (E) 500 μm microchannels + nHA and VEGF, (F) 250 μm microchannels + nHA and VEGF. 3 and 5 d HUVEC growth on scaffolds with (C) and (D) 500 μm microchannels and (G) and (H) 250 μm microchannels + nHA + VEGF.

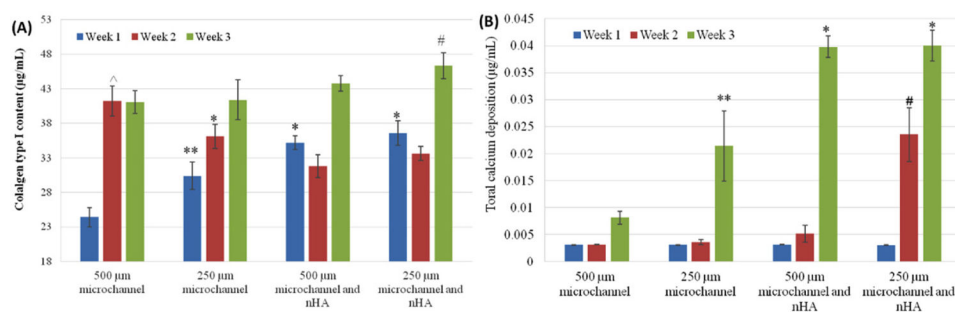


Figure 12.

(A) Enhanced type I collagen synthesis on microvascular nHA modified scaffolds after 3 weeks. Data are mean \pm standard error of the mean, $n = 9$; $^*p < 0.01$ when compared to scaffolds with 500 and 250 μm microchannels at week 1; $^{**}p < 0.05$ when compared to scaffolds with 500 μm microchannels at week 1; $^{\wedge}p < 0.05$ when compared to all other scaffolds at week 2; $^{\#}p < 0.05$ when compared to scaffolds with 500 μm microchannels at week 3. (B) Enhanced calcium deposition on microvascular nHA modified scaffolds after 3 weeks. Data are mean \pm standard error of the mean, $n = 9$; $^*p < 0.05$ when compared to 3D printed bone scaffolds with 500 and 250 μm microchannels at week 3; $^{**}p < 0.05$ when compared to 3D printed bone scaffolds with 500 μm microchannels at week 3; $^{\#}p < 0.01$ when compared to all other scaffolds at week 2.

Table 1

A table of computed and measured scaffold physical attributes.

Parameters	Measure methods	500 μm	250 μm
Porosity (%)	Computed value	41	42
	SEM measure	50	52
Volume (mm^3)	Computed value	117	105
	SEM measure	133	104
Surface area (mm^2)	Computed value	3400	3014
	SEM measure	3407	2672
Surface area/volume ratio (mm^{-1})	Computed value	29	29
	SEM measure	26	26